



# Fast and facile sonochemical synthesis of Mg- and Zn-doped PbS nanospheres: optical properties and photocatalytic activity

N. F. Andrade Neto<sup>1</sup> · O. B. M. Ramalho<sup>1</sup> · H. Fantucci<sup>2</sup> · R. M. Santos<sup>2</sup> · M. R. D. Bomio<sup>1</sup> · F. V. Motta<sup>1</sup>

Received: 6 April 2020 / Accepted: 8 July 2020 / Published online: 14 July 2020  
© Springer Science+Business Media, LLC, part of Springer Nature 2020

## Abstract

In this work, Mg<sup>2+</sup>- and Zn<sup>2+</sup>-doped PbS nanopowders were synthesized simply and quickly by a sonochemical method. The nanopowders were characterized by X-ray diffraction, wavelength dispersive X-ray fluorescence, scanning electron microscopy, and ultraviolet–visible spectroscopy. The photocatalytic activity was estimated by methylene blue dye degradation. The sonochemical method produces crystalline PbS particles with cubic structure and free of secondary phases. The use of polyvinylpyrrolidone as a surfactant, and reaction medium at pH 13, results in the formation of nanospheres with diameter ranging from 31.4 to 114.5 nm. Doping favors the absorption of radiation in the visible region, and consequently, reduces the optical bandgap of the PbS. Photocatalytic assays show that magnesium and zinc codoping results in 80% reduction of methylene blue concentration after 180 min, while undoped PbS achieves only 42%. Tests with charge scavengers indicate that holes (h<sup>+</sup>) act as the main mechanism in the photocatalytic process.

## 1 Introduction

Continued industrial development has led to increasing concern with wastewater treatment availability and effectiveness, wherein the removal or degradation of organic dyes has gained attention [1, 2]. Approximately 20% of the world's pigment production is lost during dyeing, being released as part of textile wastewater, and thus requiring treatment to protect the environment and water supply [3]. Advanced oxidative processes (AOPs), especially those applying heterogeneous photocatalysis, are widely studied as green chemistry approaches, as they generate water, carbon dioxide gas and inorganic salts from the mineralization of organic compounds [4, 5]. Such technique consists of exposing a semiconductor material to appropriate radiation in order to

excite the valence band (VB) electrons to the conduction band (CB), forming electron/hole pairs (e<sub>cb</sub><sup>-</sup>/h<sub>vb</sub><sup>+</sup>), which when in contact with an aqueous solution containing organic dye compounds generates reactive oxygen species (ROS) that have high oxidative capacity [6, 7].

Semiconductors have been studied for use in AOP due to their adaptable optical and electronic properties, whereby these properties can be readily modified by inserting defects within their crystal structure [8]. Semiconductors such as TiO<sub>2</sub> [9], CdS [10], AgCl [11], ZnO [12] and ZnS [13] have been widely studied for this purpose. Among these, nanoparticles formed of metal sulfides have been found to possess optical properties that make them suitable for diverse applications [14]. PbS is an important group IV–VI semiconductor that has been applied in various fields, including telecommunications, solar cells, biological systems, sensors, and infrared detectors [2, 15, 16]. Among the possibilities for modifying the PbS lattice, doping is attractive for its ability to control structure, morphology, and optical properties [17, 18].

PbS doping with elements such as lithium, strontium, iron, cobalt, and nickel is found in recent literature [19–21]. In addition, magnesium and zinc are doping elements that when inserted into the PbS crystal structure causes defects that improve the properties of this semiconductor; Liu et al. [22] and Gassoumi et al. [23] doped PbS thin films with zinc and magnesium, respectively, and optimized their optical

**Electronic supplementary material** The online version of this article (<https://doi.org/10.1007/s10854-020-03975-7>) contains supplementary material, which is available to authorized users.

✉ N. F. Andrade Neto  
netoandrade@ufrn.edu.br

<sup>1</sup> LSQM, Laboratory of Chemical Synthesis of Materials, Department of Materials Engineering, Federal University of Rio Grande do Norte, UFRN, P.O. Box 1524, Natal, RN, Brazil

<sup>2</sup> School of Engineering, University of Guelph, Guelph, ON N1G 2W1, Canada

properties. However, the literature lacks studies that report the photocatalytic activity of doped PbS powders, the majority having been done using thin films.

PbS nanoparticles and thin films can be synthesized by different methods, the most common of which are coprecipitation, thermal decomposition, successive ion layer adsorption and reaction (SILAR), and sonochemical [24–28]. Hines and Scholes [24] synthesized PbS nanocrystals by a coprecipitation method, first producing lead oleate precursor (at 150 °C for 1 h under inert atmosphere) that was then vigorously mixed with a solution of TMS [bis(trimethylsilyl) sulfide] at 80 to 140 °C until crystals of desired particle size formed. Sharma et al. [28] synthesized Sr- and Cd-doped PbS thin films onto cleaned glass slide substrate by the SILAR method, wherein a later stage of calcination at 120 °C is necessary to remove impurities. In contrast, the sonochemical method is a fast and simple approach that produces materials without the need for further treatment [27].

This work aims to study the structural and photocatalytic effects of the insertion of Mg and Zn ions in the PbS lattice of nanopowders (in total proportions of 4 to 8 mol%), while utilizing a sonochemical method to speed up the synthesis and to control the particle size and morphology (aiming at producing nanospheres). Codoping was tested to investigate if Mg and Zn can generate synergistic photocatalytic effect, in addition to improving the physical and chemical properties of PbS. The photocatalytic property of the resulting nanospheres was estimated by oxidative discoloration of methylene blue dye solution, when illuminated by UV radiation. An active species scavenging methodology was applied for investigation of the mechanisms governing the photocatalytic activity of undoped and doped PbS nanopowders.

## 2 Materials and methods

### 2.1 Synthesis

PbS nanopowders, undoped and doped, were prepared using lead nitrate [Pb(NO<sub>3</sub>)<sub>2</sub>, Sigma-Aldrich, 99%], thiourea (CH<sub>4</sub>N<sub>2</sub>S, Synth, 99%), zinc nitrate [Zn(NO<sub>3</sub>)<sub>2</sub>, Sigma-Aldrich, 98%], magnesium nitrate [Mg(NO<sub>3</sub>)<sub>2</sub>, Sigma-Aldrich, 99%], polyvinylpyrrolidone polymer (PVP, Alfa Aesar, MW = 40.000), sodium hydroxide (NaOH, Synth, 98%), and deionized water. For this, 4 mmol of lead nitrate was added to 50 mL of deionized water and kept under stirring; after complete dissolution, 4 mmol of thiourea, as the source of reduced sulfur, was added. After 10 min of further stirring, a second solution containing 30 mL of deionized water and 1 g of dissolved sodium hydroxide was added, to fix the pH to 13.0. The combined solution then remained under stirring for another 30 min. Subsequently, the solution was placed under an ultrasonic probe

tip ( $\varnothing = 13$  mm) coupled to a converter (model Branson 102-C, 20 kHz) and processor (model Branson SFX250 Sonifier, 250 W), where it remained for 30 min at 70% nominal amplitude. After this time, the precipitate was centrifuged and washed with DI water. The doped samples were obtained similarly, but with the addition of zinc and/or magnesium nitrate, stoichiometrically in the proportions of 4 or 8 mol% replacing lead nitrate; these proportions are based on our previous work that thus showed the best optical properties [27]. The samples were named according to their molar ratio, namely P4M, P4Z, and P4MZ for the 4 mol% samples, and P8M, P8Z and P8MZ for the 8 mol% samples, where M is magnesium and Z is zinc. For the mixed doped samples (i.e., MZ), the mol% proportion (4 or 8) was the total of the two dopants at an equal ratio.

### 2.2 Characterization

X-ray diffraction (XRD) analysis was performed on a Shimadzu XRD-6000 diffractometer using Cu K $\alpha$  (1.5418 Å) radiation, to identify the crystalline phases of the nanopowders. Rietveld refinement was performed using GSAS software with the EXPGUI interface [29], to analyze possible microstructural changes in the PbS lattice when doping with Mg<sup>2+</sup> and Zn<sup>2+</sup>.

The elemental composition of the nanopowders was quantified by wavelength dispersive X-ray fluorescence (WDXRF, Malvern Panalytical Zetium). For this, loose powder samples were analyzed for 20 min using the standardless Omnium method, under helium and at 1 kW power. Elemental concentrations were quantified in SuperQ v6 (Malvern Panalytical) using drift correction, finite thickness model, and values were normalized to 100% using Pb as the balance element (sum before normalization ranged from 11.6 to 16.1 wt%, with precision determined from replicates as  $\pm 0.1$  wt%).

Field emission scanning electron microscopy (FE-SEM) was performed for observation of particle morphology in a Carl Zeiss microscope (Auriga). Energy-dispersive X-ray (EDX) spectroscopy was performed for chemical identification of the nanopowders using a Zeiss SmartEDX spectrometer. Image analysis was performed to determine particle size distribution (based on 100 counts, in triplicate, per sample) using ImageJ software (U.S. National Institutes of Health).

UV–Vis spectroscopy (UV–Vis) was conducted on a Shimadzu UV-2550 equipment, operating in diffuse reflectance mode with wavelength ranging from 200 to 900 nm. Reflectance data were converted to absorbance by the Kubelka–Munk function [30], and the Wood and Tauc equation [31] was applied to obtain the optical band gap ( $E_{\text{gap}}$ ) of the nanopowders.

### 2.3 Photocatalytic properties

The photocatalytic properties were estimated by the oxidative discoloration of methylene blue dye (Mallinckrodt, 99.5% purity and  $10^{-5}$  mol L<sup>-1</sup> concentration) under UV radiation. For this, 50 mL of methylene blue dye (MB) was kept under stirring with 0.05 g of nanopowder. The nanopowders were initially kept in contact with MB dye for 30 min to eliminate adsorptive effects; a sample was taken every 10 min and its UV–Vis absorbance was measured. UV illumination was then performed by placing the solution under six UVC lamps (TUV Philips, 15 W, 240–260 nm wavelength). For discoloration analysis, a sample was taken every 30 min and its UV–Vis absorbance was measured.

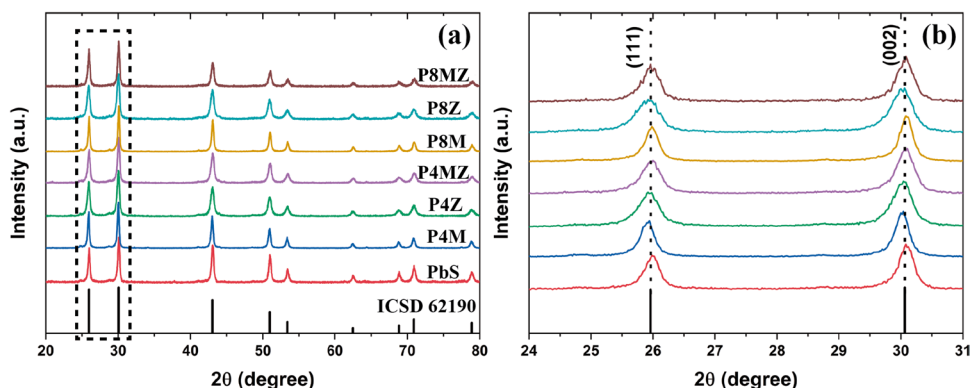
The photocatalytic mechanisms acting on the oxidative process were studied by applying the principle of active species scavenging [32]. In this methodology, compounds are added to the MB solution that impairs the efficacy of certain active species during UV illumination. For this, 0.5 mL isopropyl alcohol (Sigma-Aldrich, 99.7%), 3.6 mg EDTA (97%, Sigma-Aldrich) and 4.3 mg de AgNO<sub>3</sub> (Synth, 99%), added to 50 mL of dye solution with 0.05 g of nanopowder, were used as scavengers against hydroxyl radical ( $\cdot\text{OH}$ ), positive charges ( $\text{h}^+$ ), and negative charges ( $\text{e}^-$ ), respectively.

### 3 Results and discussion

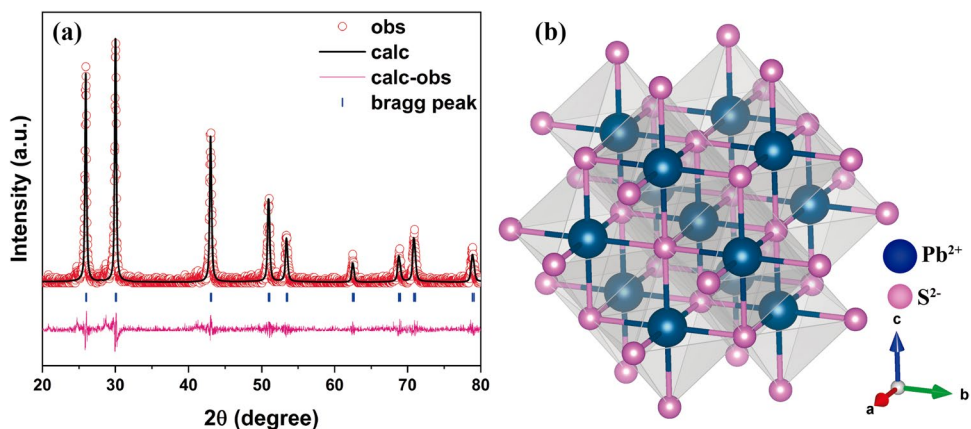
Figure 1 shows the diffractograms for undoped and Mg<sup>2+</sup>- and Zn<sup>2+</sup>-doped PbS. The crystalline arrangement is characterized based on the ICSD Card 62190 to be of cubic structure and space group *Fm-3m*. As previously reported in literature by Behboudnia et al. [33], sonication does not result in alteration of crystal structure. No secondary peak formation is observed, indicating the correct incorporation of Mg<sup>2+</sup> and Zn<sup>2+</sup> ions into the PbS lattice. Figure 1b shows the magnification of the main peaks relative to the (111) and (002) planes. The peaks shift in regard to the ICSD Card 62190, indicating changes in crystal structure due to doping. According to Yoo et al. [34], diffraction peak displacement occurs due to changes in interplanar spacing (e.g., reductions in spacing promote peak displacement to greater diffraction angles). Doping is thus expected to result in an asymmetric broadening of pure-phase peaks; such observation is further evidence of the incorporation of the doping elements into the PbS structure.

Figure 2a presents the calculated diffractogram obtained through Rietveld refinement for the undoped PbS sample, while Fig. 2b illustrates its cubic structure, obtained with the aid of VESTA software [35]. The cubic structure is formed

**Fig. 1** **a** Diffractograms for the PbS samples, and **b** highlighted section with the (111) and (002) planes



**Fig. 2** **a** Observed and calculated diffractograms curves obtained by the Rietveld refinement, and **b** crystallite structure simulated by VESTA software



with  $\text{Pb}^{2+}$  atoms attached to six  $\text{S}^{2-}$  atoms. Table 1 presents the crystallographic data obtained through the Rietveld refinement for undoped and doped PbS. According to Table 1, there is a reduction in the crystallite size and lattice parameters as the dopant concentration is increased, which is characteristic of substitutional doping [36, 37]. These reductions occur due to increasing the number of defects and the differences between the ionic radii;  $\text{Pb}^{2+}$ ,  $\text{Mg}^{2+}$ , and  $\text{Zn}^{2+}$  cations possess radii of 1.19, 0.72, and 0.74 Å, respectively [27]. According to Liu et al. [38],  $\text{Zn}^{2+}$  atoms can replace  $\text{Pb}^{2+}$  when they are in the  $\text{Pb-S}_6$  coordination octahedron, replacing the  $\text{Pb-S}$  (0.297 nm) bonds with  $\text{Zn-S}$  (0.278 nm) bonds, and consequently reducing the lattice parameter. Nakrela et al. [36] pointed that substitutional doping by smaller ions is predicted by Vegard's law to result in appreciable shrinking of the lattice, while for interstitial doping, the lattice would expand.

Further confirmation of the incorporation of Mg and Zn ions in the PbS lattice was obtained through chemical analysis by WDXRF, to quantitatively confirm that the desired Mg/Pb, Zn/Pb and Mg/Zn molar ratios were present in the produced samples. Table 2 shows the theoretical (i.e., stoichiometry-based) and measured values for Mg and Zn molar concentrations, and Figs. S1, S2, S3 and S4 (Supplementary Information) show the WDXRF spectra for undoped PbS, and doped P4M, P4Z and P4MZ samples, which have the smallest doping compositions (4 mol%). According to data shown in Table 2, the theoretical and measured concentrations are similar, and within the expected uncertainty of the standardless semi-quantitative method used, serving to confirm the intended incorporation of the desired quantities of Mg and Zn ions into the PbS lattice.

Figure 3a–g shows the micrographs obtained for the undoped and Mg- and Zn-doped PbS samples. According to the micrographs, the predominance of semi-spherical morphology, with some aggregation as expected for uncoated nanoparticles due to Van de Waals attraction, is noticed. Compared to similar morphology reported in literature [39, 40], these nanopowders are deemed to be composed of aggregated nanospheres, which also can be referred to as nanoclusters made up of spherical crystallites [33]. The morphology obtained can be attributed to

**Table 2** Theoretical and calculated values by the WDXRF method for the magnesium and zinc composition of doped PbS nanopowders

Samples	Theoretical (mol%)		Measured (mol%)	
	Mg	Zn	Mg	Zn
P4M	4.00	0	3.58 ( $\pm 0.19$ )	0
P4Z	0	4.00	0	3.07 ( $\pm 0.11$ )
P4MZ	2.00	2.00	2.7 ( $\pm 0.19$ )	1.88 ( $\pm 0.07$ )
P8M	8.00	0	6.53 ( $\pm 0.28$ )	0
P8Z	0	8.00	0	5.72 ( $\pm 0.14$ )
P8MZ	4.00	4.00	4.17 ( $\pm 0.19$ )	3.43 ( $\pm 0.10$ )

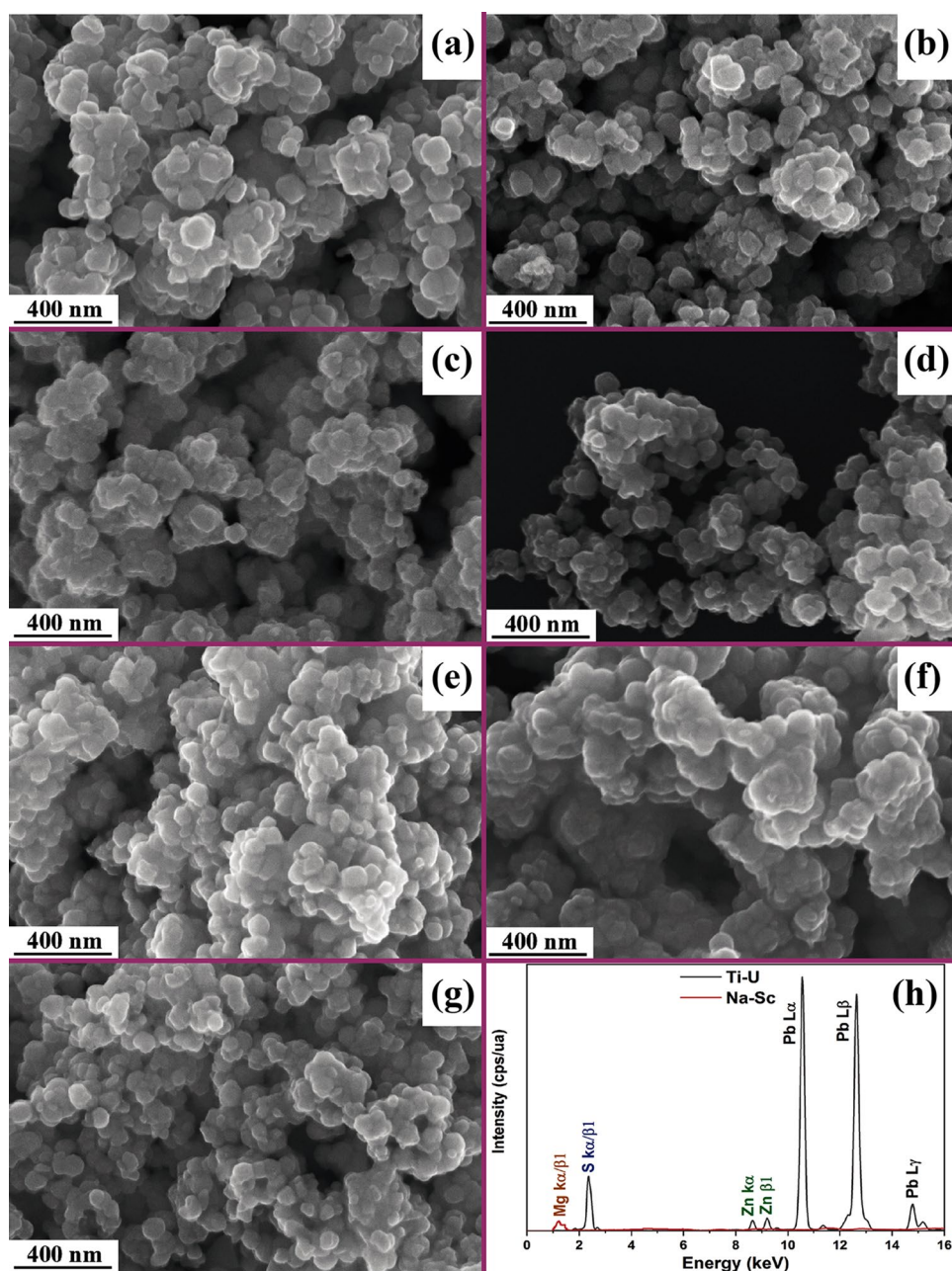
the surfactant and the sonochemical method used. The PVP was used as a surfactant for morphological control, because of its intrinsic non-ionic character and non-toxicity [41]. The PVP chains, combined with their non-ionic character, act to suppress the growth of particles in all directions, inducing the formation of semi-spherical nanoparticles [42]. The sonochemical methodology is characterized by the supply of ultrasonic waves to the system through the formation and implosion of cavities, which create localized zones of elevated pressure and temperature. These effects, together with the PVP surfactant, favor nucleation over crystal growth, thus leading to the formation of nanoparticles and prevention of excessive growth of particles [43]. Nanoparticles have high surface energy, thus to reduce it they favor spherical morphology [44].

Figure 3h shows the EDX spectra corresponding to the P4MZ micrograph. EDX analysis was used to qualify the chemical composition, in support of the semi-quantitative WDXRF results, and the presence of both dopants is detected, with no visible secondary phases of altered composition detected. Wang et al. [45] noted that  $\text{Pb}^{2+}$  tends to absorb on the surface of PbS nanocrystals, which were sonochemically prepared in that study, and this results in a Pb:S molar ratio greater than 1. They found through EDX analysis (which is surface sensitive) that this ratio is 1.155, and by X-ray photoelectron spectroscopy (XPS) to be 1.19. Conversely, Zhu et al. [46] reported Pb:S molar ratios lower than 1 (0.754 from EDX and XPS analyses),

**Table 1** Crystalline and quality parameters of the Rietveld refinement obtained through the GSAS software

Sample	PbS	P4M	P4Z	P4MZ	P8M	P8Z	P8MZ
$a$ (Å)	5.9418	5.9413	5.9409	5.9382	5.9412	5.9398	5.9379
Cell volume (Å <sup>3</sup> )	209.77	209.72	209.68	209.39	209.71	209.56	209.36
Crystallite size (nm)	25.65	19.22	23.85	20.88	17.35	21.31	20.28
Microstrain ( $10^{-4}$ )	3.27	3.01	4.36	4.02	2.96	4.82	3.76
$\chi^2$	1.238	1.298	1.365	1.386	1.329	1.369	1.389
$R_{wp}$	0.3084	0.3062	0.1814	0.3152	0.2815	0.1816	0.3181
$R_p$	0.2190	0.2186	0.2181	0.2348	0.1995	0.2190	0.2451

**Fig. 3** SEM micrographs for the **a** PbS, **b** P4M, **c** P4Z, **d** P4MZ, **e** P8M, **f** P8Z and **g** P8MZ samples; and **h** EDX spectra for the P4MZ sample



again for sonochemically prepared PbS nanoparticles, but do not offer an explanation of the deviation from 1.

Figure 4 shows particle size distribution histograms for undoped and doped PbS nanopowders, determined from micrograph image analysis. According to the histograms and mean particle sizes, Mg doping provides a reduction in the average diameter of PbS nanoparticles; this is the case, in order from largest to smallest for P4M, P4MZ, P8MZ, and P8M, but is most significant in the case of P8M, where mean particle size reduces from 93.05 to 31.41 nm. Conversely, the introduction of zinc alone (P4Z and P8Z) increases the average diameter of the nanospheres. Liu et al. [38] have reported that the introduction of zinc ions into PbS during

thin-film deposition induces a reduction in the size of their pyramidal grains, accompanied by rounding of their vertices, and consequently contributed to thinner and smoother doped films. The sonochemical conditions here may have masked any size reduction effect of zinc, but such effects are clearly seen for magnesium doping.

Figure 5a shows the UV–Vis absorption curves for undoped and Mg- and Zn-doped PbS nanopowders. Absorption curves were obtained by applying the Kubelka–Munk equation [30] to the diffuse reflectance data. According to Fig. 5a, PbS has maximum absorption in the ultraviolet region, with two well-defined bands near 250 and 350 nm, followed by two smaller absorption bands in the visible

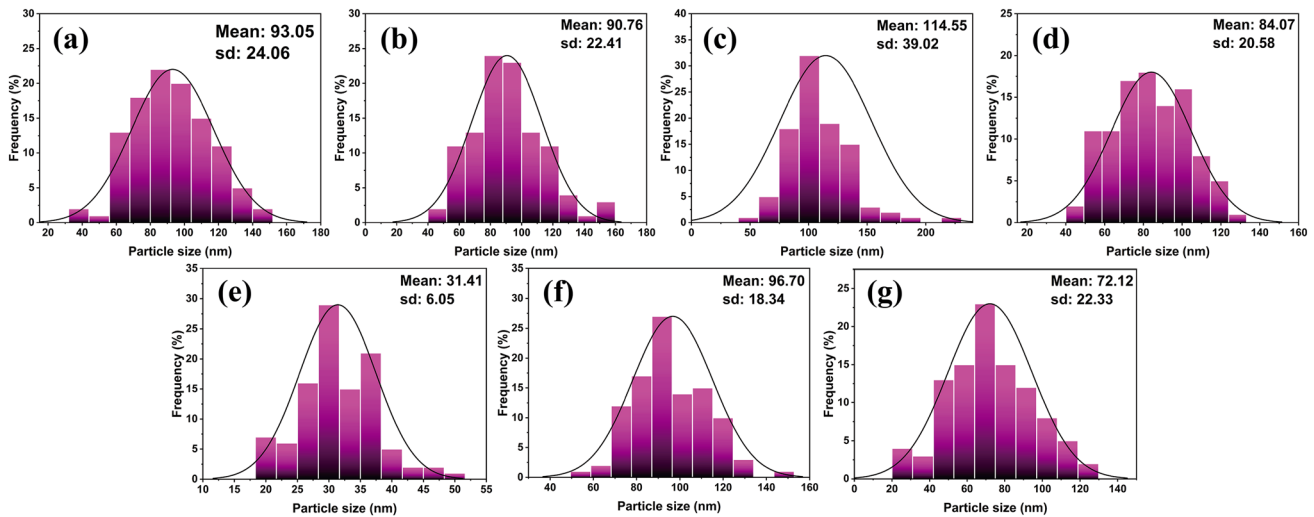


**Fig. 4** Histograms of particle size for the **a** PbS, **b** P4M, **c** P4Z, **d** P4MZ, **e** P8M, **f** P8Z, and **g** P8MZ samples

region, around 580 and 750 nm. According to Molaei et al. [47], the presence of bands in the ultraviolet region due to quantum confinement effects related to the nanoscopic scale of the material.  $Mg^{2+}$  doping reduces absorption in the ultraviolet region, leaving only one band at 340 nm, and increases absorption in the visible region, producing a wide band centered around 600 nm. As  $Mg^{2+}$  concentration increases from 4 to 8 mol%, a reduction in the 350 nm band and an increase in the 600 nm band can be seen.

Doping with 4 mol%  $Zn^{2+}$  also acts to reduce absorption in the ultraviolet region, reducing the band at 350 nm, while leading to the appearance of a small band around 225 nm, and producing increased absorption in the visible region, though less so than with  $Mg^{2+}$  doping. With the doping amount of  $Zn^{2+}$  at 8 mol%, absorption in the visible region reverses back to level similar to that of undoped PbS. Parallel to this, there is increased absorption in the ultraviolet region compared to undoped PbS, at 250 and 350 nm.

Codoping at 4 mol% results in the modification and displacement of absorption bands. For the ultraviolet region, small bands appear at 250 and 275 nm, while in the visible region there is increased absorption, with a wide band centered around 590 nm. Increasing the codoping to 8 mol% increases the intensity of these bands, and leads to a further band shift in the visible region (now centered around 560 nm).

The increased absorption that occurs with doping is associated with the appearance of intermediate levels in the forbidden PbS band, allowing the absorption of greater wavelength radiation [48]. The intermediate levels eventually

generate several forms of recombination between  $e^-/h^+$  pairs, the most common being (I) recombination of  $e^-/h^+$  pairs near the bands; (II) electrons from Pb and holes in the valence band; (III) Pb empty bond electrons and holes in the S-bond; and (IV) electrons in the conduction band and holes in the S-bond [47, 49].

Figure 5b shows the curves of  $\alpha^2$  variation, where  $\alpha$  is the absorption coefficient of the material, versus photon energy, obtained by the Wood and Tauc equation [50, 51]. The  $E_{gap}$  is obtained by extrapolating the linear portion of the  $\alpha^2$  curves. Table 3 presents the estimated values of direct  $E_{gap}$ , and the error and coefficient of determination ( $R^2$ ) associated to the extrapolation of the linear portion of the  $\alpha^2$  curves. According to  $R^2$  values, linear fitting is well adjusted to the selected portion of the curves.

$E_{gap}$  is directly related to the presence of defects in the crystal lattice and the morphology of materials [7]. As discussed earlier, doping provides increased absorption in the visible region, indicating a reduction in  $E_{gap}$  [52]. The samples codoped, both with 4 mol% and 8 mol%, showed more significant increase in  $E_{gap}$  than the samples with single dopants. However, even with single dopants, samples with Mg doping showed greater  $E_{gap}$  than samples with Zn doping. These effects may be associated with the Burstein–Moss effect, where Mg occupies states near the conduction band, shifting it to higher energy states [53]. According to Liu et al. [38], the increase in  $E_{gap}$  for PbS through doping may occur due to quantum confinement, shifting the absorption band to higher frequencies. Changes in  $E_{gap}$ , in parallel with morphological, chemical and crystallographic changes,

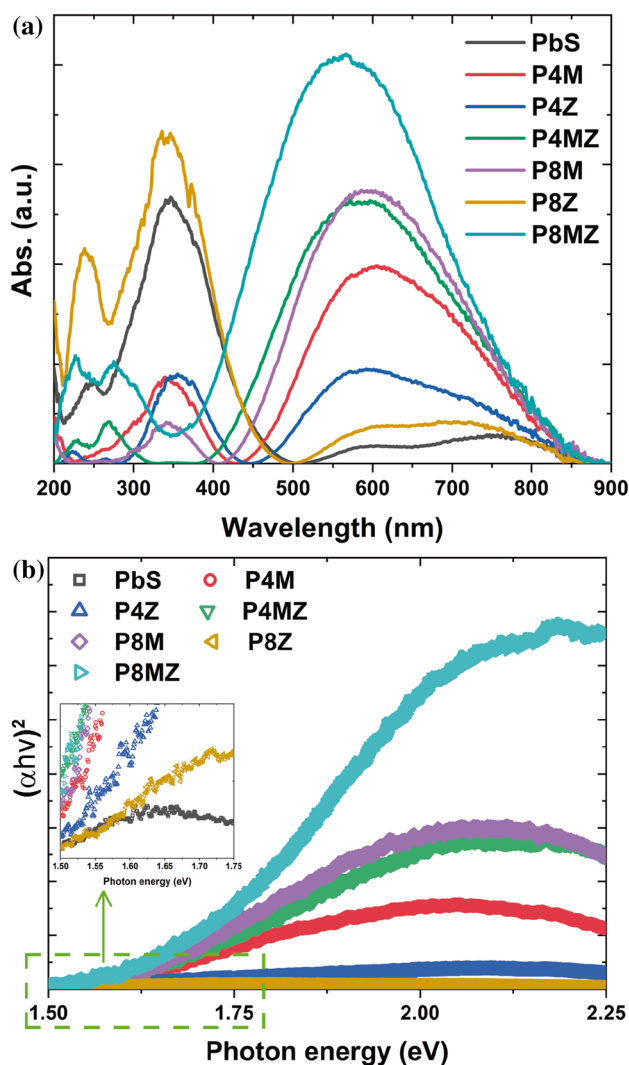


**Fig. 5** **a** UV–Vis absorption curves obtained by Kubelka–Munk methodology, and **b** direct transitions curves obtained by Wood and Tauc equation

confirm the successful introduction of  $\text{Mg}^{2+}$  and  $\text{Zn}^{2+}$  ions into PbS lattice through the sonochemical method employed, and exemplify the benefit of codoping.

Figure 6 shows the concentration curves of MB versus the assay time for the photocatalytic dye degradation experiments. The photolysis curve corresponds to the analysis without the presence of a catalyst, indicating that UV radiation reduces the MB concentration by only about 7%

after 180 min of illumination. To quantify the photocatalytic activity of PbS nanopowders, first-order modeling was performed, based on the Fig. 6 data, to obtain the kinetic constants. Similarly, adsorption reaction constants were determined based on initial MB concentration and equilibrium MB concentration after 30 min, before UV illumination. According to Santiago et al. [54], the kinetic constant can be obtained by

$$k = \frac{-\ln(C_t/C_0)}{t}, \quad (1)$$

where  $k$  is the first-order kinetic constant,  $t$  the test time,  $C_t$  the concentration at time  $t$ , and  $C_0$  the initial concentration.

Catalytic and adsorption kinetics is strongly dependent on medium concentration, whereby the higher the concentration of dye molecules in the medium, the higher the initial rate [55]. As shown in Table 4, the PbS sample has the lowest kinetic constant for adsorption and photocatalysis, indicating that Mg and Zn doping increases the rate of MB removal via both mechanisms.

The P4MZ sample had the highest adsorptive capacity (pre-illumination), reducing approximately 25% of the concentration of MB dye; other doped samples resulted in 10% to 20% adsorption, versus 5% for undoped PbS. As discussed earlier, doping generates many material defects, shifting the conduction band to higher energy states and favoring negative charge defects on the surface of the particles. Due to the cationic character of the MB dye, such defects act to facilitate the adsorption of these molecules to the surface of PbS nanospheres. The improvement in adsorption effect is also associated with alterations on the surface of the particles, as shown in SEM micrographs, where the doping generates a reduction in particle size.

Ajibade and Oluwalana [56] produced capped PbS nanoparticles with a quasi-spherical morphology, with a medium diameter of 17.25 nm, and used them to degrade approximately 66% of MB dye concentration after 180 min, while in this work for the P4Z (114.55 nm) and P8Z (96.70 nm) samples degraded over 70% of MB dye, and P8M (31.41 nm) and P8MZ (72.12 nm) degraded close to 80% of MB dye, with the same duration. Improvement in photocatalytic properties of materials with doping is reported in several papers [57–59]. These improvements are due to the differences between solvent and solute, usually associated with ionic radius and valence, which generate defects that act

**Table 3** Direct  $E_{\text{gap}}$  estimated by the Wood and Tauc methodology

Samples	PbS	P4M	P4Z	P4MZ	P8M	P8Z	P8MZ
$E_{\text{gap}}$ (eV)	1.48	1.56	1.50	1.59	1.60	1.50	1.67
Error	0.06	0.03	0.06	0.02	0.02	0.06	0.02
$R^2$	0.998	0.994	0.996	0.997	0.997	0.996	0.997

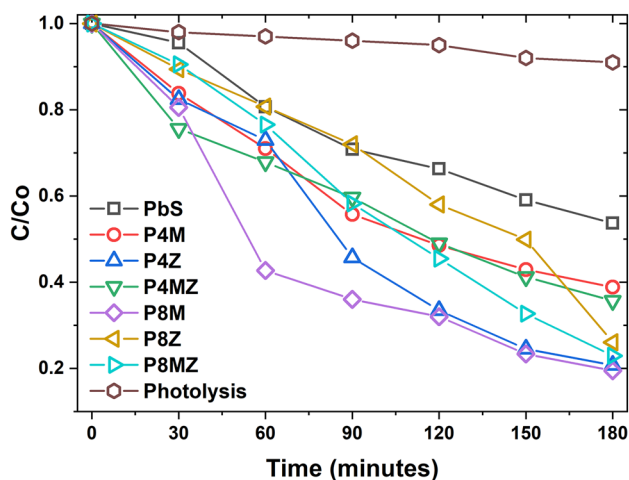


**Fig. 6** Curves of methylene blue dye concentration as a function of UV illumination time; time zero represents 30 min of adsorption equilibration prior to illumination

to prevent the recombination of electron/hole pairs ( $e^-/h^+$ ), leaving more ROS available to act on the degradation of dye molecules [60].

Our previous work [27] showed that the photocatalytic activity of the PbS is improved as a function of increasing Ag doping, where the catalytic kinetic constant increased from 1.69 (bare PbS) to  $7.57 \text{ min}^{-1}$  (for 8% Ag-doped PbS). As shown in Table 4, the catalytic kinetic constant increases from 3.56 (bare PbS, sonochemically produced) to  $10.76 \text{ min}^{-1}$  (8% Zn-doped PbS), indicating that Zn enhances the photocatalytic activity against Ag. The chemical stability of the nanopowders was analyzed by XRD after the photocatalytic tests. The diffractograms in Fig. S5 (Supplementary Information) show that there is no formation of secondary phases, indicating the stability of the PbS after the photocatalytic process.

To better understand the photocatalytic dye degradation mechanisms that the doping of  $\text{Mg}^{2+}$  and  $\text{Zn}^{2+}$  atoms into the PbS lattice generates, the active species scavenging methodology was applied to the PbS, P8M, and P8Z samples. Figure 7

shows MB dye concentration curves illustrating the effect of charge hijackers on the degradation extent. For all samples tested,  $\text{AgNO}_3$  addition promotes the optimization of photocatalytic activity, versus the case without scavengers, while adding EDTA and isopropyl alcohol reduces catalytic efficiency.  $\text{AgNO}_3$  acts to suppress free electrons, so that it prevents recombination with the holes ( $h^+$ ), which migrate to the surface and when in contact with the aqueous medium generate ROS having high oxidative capacity against organic dyes [61]. On the other hand, EDTA suppresses the holes ( $h^+$ ) generated by electronic excitation, making impossible the ROS generation and consequently reducing the photocatalytic capacity of PbS [61, 62]. A similar effect occurs when adding isopropyl alcohol, where it acts to suppress the action of hydroxyl radicals ( $\cdot\text{OH}$ ) generated during the reaction between holes ( $h^+$ ) and water molecules [62]. Thus, it can be assumed that the photocatalytic activity of undoped and Mg- and Zn-doped PbS is directly related to ROS generation in the reaction medium.

## 4 Conclusion

The sonochemical method is fast and efficient to obtain PbS nanoparticles with nanospherical morphology and without the formation of secondary phases, for doping with 4 and 8 mol% of  $\text{Zn}^{2+}$  and  $\text{Mg}^{2+}$ , singly or combined. The high crystallinity of the samples indicates that it is not necessary to perform further preparation steps after the sonochemical treatment. Doping with  $\text{Mg}^{2+}$  and  $\text{Zn}^{2+}$  proved to be efficient to optimize the optical properties of PbS nanopowders, increasing the absorption in the visible region. The photocatalytic activity is strongly influenced by the impediment of electron/hole pairs' recombination, which provides more holes ( $h^+$ ) available on the surface of the PbS particles, and consequently increases the generation of reactive oxygen species, which have a high capacity for degrading organic contaminants. Thus,  $\text{Mg}^{2+}$ - and  $\text{Zn}^{2+}$ -doped PbS nanopowders are a promising new class of materials for optical and photocatalytic applications against organic contaminants that are difficult to treat by conventional methodologies.

**Table 4** Kinetic constants of photocatalysis and adsorption for undoped and doped PbS nanopowders

Samples	PbS	P4M	P4Z	P4MZ	P8M	P8Z	P8MZ
$k_{\text{ads}} \times 10^{-3} (\text{min}^{-1})$	1.526	5.894	6.444	9.324	7.211	3.731	3.318
$k_{\text{cat}} \times 10^{-3} (\text{min}^{-1})$	3.561	5.824	8.237	5.954	4.772	10.758	6.530



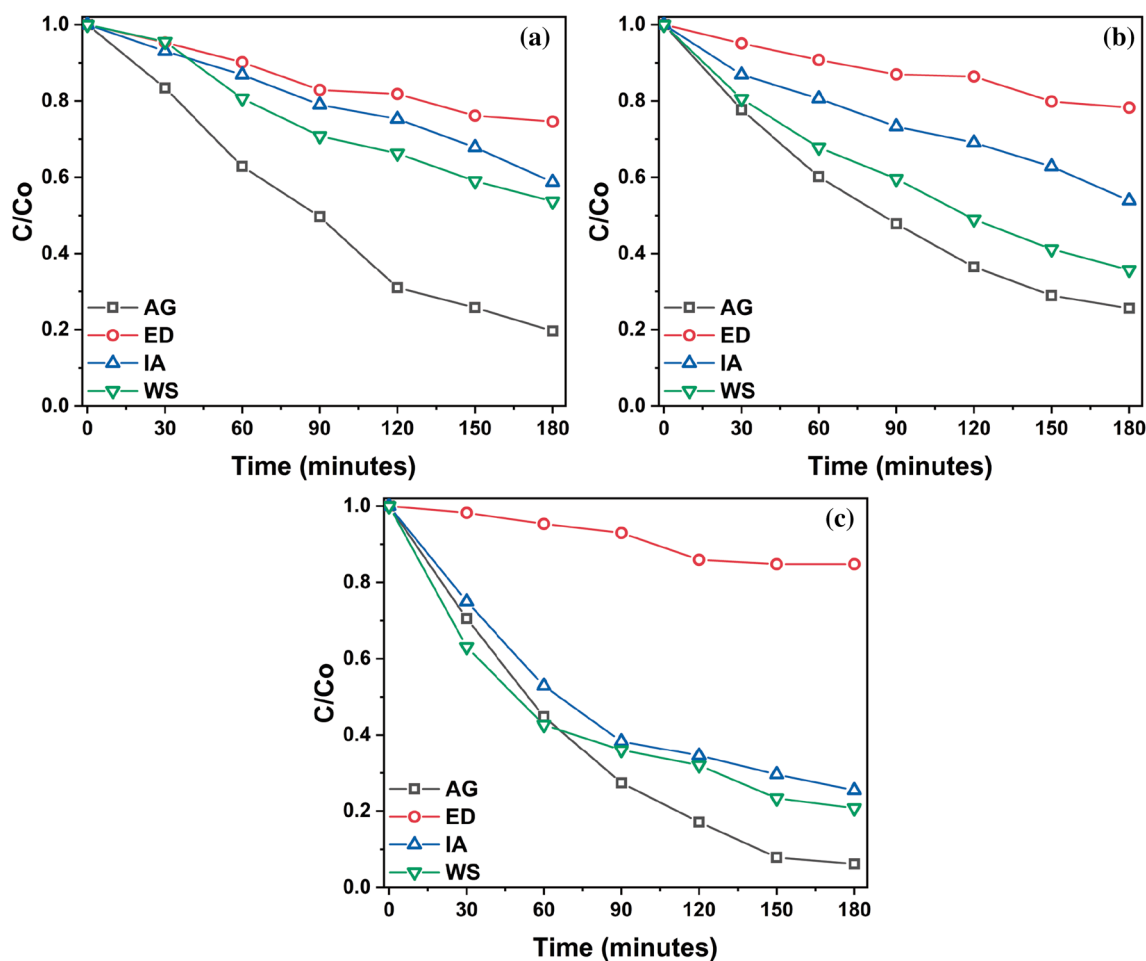


**Fig. 7** Curves of methylene blue dye concentration as a function of UV illumination time in the presence of scavengers (AG=AgNO<sub>3</sub>; ED=EDTA; IA=isopropyl alcohol) and without scavengers (WS) for the **a** PbS, **b** P8M and **c** P8Z samples

**Acknowledgement** This study was financed in part by the Coordenação de Aperfeiçoamento de Pessoal de Nível Superior, Brasil (CAPES/PROCAD): Finance Code 2013/2998/2014 and Finance Code 001. The authors thank the financial support of the Brazilian research financing institution: CNPq No. 307546/2014, and the technical support of the Natural Sciences and Engineering Research Council of Canada, RGPIN-201904839.

## References

1. M. Babaahamdi-Milani, A. Nezamzadeh-Ejhieh, A comprehensive study on photocatalytic activity of supported Ni/Pb sulfide and oxide systems onto natural zeolite nanoparticles. *J. Hazard. Mater.* **318**, 291–301 (2016)
2. V.R. Raja, D.R. Rosaline, A. Suganthi, M. Rajarajan, Facile fabrication of PbS/MoS<sub>2</sub> nanocomposite photocatalyst with efficient photocatalytic activity under visible light. *Solid State Sci.* **67**, 99–108 (2017)
3. M. Nasirian, C.F. Bustillo-Lecompte, M. Mehrvar, Photocatalytic efficiency of Fe<sub>2</sub>O<sub>3</sub>/TiO<sub>2</sub> for the degradation of typical dyes in textile industries: effects of calcination temperature and UV-assisted thermal synthesis. *J. Environ. Manag.* **196**, 487–498 (2017)
4. C.M. Malengreux, S.L. Pirard, G. Léonard, J.G. Mahy, M. Herlitschke, B. Klobes, R. Hermann, B. Heinrichs, J.R. Bartlett, Study of the photocatalytic activity of Fe<sup>3+</sup>, Cr<sup>3+</sup>, La<sup>3+</sup> and Eu<sup>3+</sup> single-doped and co-doped TiO<sub>2</sub> catalysts produced by aqueous sol-gel processing. *J. Alloys Compd.* **691**, 726–738 (2017)
5. M.I. Litter, Heterogeneous photocatalysis: transition metal ions in photocatalytic systems. *Appl. Catal. B* **23**, 89–114 (1999)
6. M. Rauf, S.S. Ashraf, Fundamental principles and application of heterogeneous photocatalytic degradation of dyes in solution. *Chem. Eng. J.* **151**, 10–18 (2009)
7. N.F. Andrade Neto, K.N. Matsui, C.A. Paskocimas, M.R.D. Bomio, F.V. Motta, Study of the photocatalysis and increase of antimicrobial properties of Fe<sup>3+</sup> and Pb<sup>2+</sup> co-doped ZnO nanoparticles obtained by microwave-assisted hydrothermal method. *Mater. Sci. Semicond. Process.* **93**, 123–133 (2019)
8. N.F. Andrade Neto, P. Zanatta, L.E. Nascimento, R.M. Nascimento, M.R.D. Bomio, F.V. Motta, Characterization and photoluminescent, photocatalytic and antimicrobial properties of boron-doped TiO<sub>2</sub> nanoparticles obtained by microwave-assisted solvothermal method. *J. Electron. Mater.* **48**, 3145–3156 (2019)
9. E. Craciun, L. Predoana, I. Atkinson, I. Jitaru, E.M. Anghel, V. Bratan, C. Gifu, C. Anastasescu, A. Rusu, V. Raditoiu, Fe<sup>3+</sup>-doped TiO<sub>2</sub> nanopowders for photocatalytic mineralization of oxalic acid under solar light irradiation. *J. Photochem. Photobiol. A* **356**, 18–28 (2018)

10. K. Deka, M.P. Kalita, Structural phase controlled transition metal (Fe Co, Ni, Mn) doping in CdS nanocrystals and their optical, magnetic and photocatalytic properties. *J. Alloys Compds.* **757**, 209–220 (2018)
11. N.A. Neto, L. Garcia, E. Longo, M. Li, C. Paskocimas, M. Bomio, F. Motta, Photoluminescence and photocatalytic properties of Ag/AgCl synthesized by sonochemistry: statistical experimental design. *J. Mater. Sci. Mater. Electron.* **28**, 12273–12281 (2017)
12. M. Sathya, K. Pushpanathan, Synthesis and optical properties of Pb doped ZnO nanoparticles. *Appl. Surf. Sci.* **449**, 346–357 (2018)
13. M. Ashokkumar, A. Boopathyraja, Structural and optical properties of Mg doped ZnS quantum dots and biological applications. *Superlattices Microstruct.* **113**, 236–243 (2018)
14. K. Hedayati, M. Kord, M. Goodarzi, D. Ghanbari, S. Gharigh, Photo-catalyst and magnetic nanocomposites: hydrothermal preparation of core-shell Fe<sub>3</sub>O<sub>4</sub>@PbS for photo-degradation of toxic dyes. *J. Mater. Sci. Mater. Electron.* **28**, 1577–1589 (2017)
15. Z.Q. Mamiyev, N.O. Balayeva, Preparation and optical studies of PbS nanoparticles. *Opt. Mater.* **46**, 522–525 (2015)
16. Y.V. Reddy, T.M. Kumar, T. Shekharam, M. Nagabhushanam, Low temperature DC electrical conductivity studies of Pb<sub>1-x</sub>Zn<sub>x</sub>S semiconductor compounds. *Solid State Sci.* **82**, 29–33 (2018)
17. Y.-L. Lu, S. Dong, B. Zhou, S. Dai, H. Zhao, P. Wu, Tuning electronic and magnetic properties of V-, Cr-, and Mn-doped PbS via strain engineering: a first-principles proposal. *Mater. Sci. Eng. B* **228**, 1–6 (2018)
18. E. Yücel, Y. Yücel, Effect of doping concentration on the structural, morphological and optical properties of Ca-doped PbS thin films grown by CBD. *Optik* **142**, 82–89 (2017)
19. M.C. Portillo, J.A. Pulido, S.G. Hernández, B.S. Cruz, S.A. Iniesta, R.G. Pérez, O.P. Moreno, V<sub>oc</sub> enhancement of a solar cell with doped Li<sup>+</sup>-PbS as the active layer. *Superlattices Microstruct.* **118**, 137–144 (2018)
20. M. Suganya, S. Anitha, D. Prabha, S. Balamurugan, J. Srivind, A. Balu, Enhanced photocatalytic and antifungal properties of Sr-doped PbS nanopowders. *Mater. Technol.* **33**, 214–219 (2018)
21. Y.-L. Lu, S. Dong, W. Zhou, Y. Liu, H. Zhao, P. Wu, Influences of isotropic strain on the electronic and magnetic properties of Fe-, Co-, and Ni-doped PbS revealed by density functional calculations. *Mater. Chem. Phys.* **223**, 133–139 (2019)
22. M. Liu, W. Li, Y. Wang, Q. He, Fabrication, characterization and simulation of Zn-doped PbS nanopowder. *Phys. B* **545**, 245–249 (2018)
23. A. Gassoumi, S. Alleg, N. Kamoun-Turki, Influencing the structural, microstructural and optical properties of PbS nanocrystalline thin films by Mg<sup>2+</sup> doping. *J. Mol. Struct.* **1116**, 67–71 (2016)
24. M.A. Hines, G.D. Scholes, Colloidal PbS nanocrystals with size-tunable near-infrared emission: observation of post-synthesis self-narrowing of the particle size distribution. *Adv. Mater.* **15**, 1844–1849 (2003)
25. X. Zheng, S. Das, Y. Gu, S. Liu, J. Zhao, Optimal engineering of CdS/PbS co-sensitized TiO<sub>2</sub> nanotube arrays for enhanced photoelectrochemical performance. *Ceram. Int.* **46**(8B), 12050–12058 (2020)
26. R. Gaur, Morphology dependent activity of PbS nanostructures for electrochemical sensing of dopamine. *Mater. Lett.* **264**, 127333 (2020)
27. N.F. Andrade Neto, Y.G. Oliveira, C.A. Paskocimas, M.R.D. Bomio, F.V. Motta, Increase of antimicrobial and photocatalytic properties of silver-doped PbS obtained by sonochemical method. *J. Mater. Sci. Mater. Electron.* **29**, 19052–19062 (2018)
28. S. Sharma, A. Venkata Dhanunjaya Reddy, N. Jayarambabu, N. Vikram Manoj Kumar, A. Saineetha, S. Kailasa, K. Venkateswara Rao, Micro-structural, optical and vibrational spectra analysis of lead sulphide, cadmium doped PbS and strontium doped PbS nano-structured thin films synthesized through successive ionic layer adsorption and reaction technique for solar cell and infrared detector sensor applications. *Mater. Today Proc.* **26**(1), 162–171 (2019)
29. B. Toby, EXPGUI, a graphical user interface for GSAS. *J. Appl. Crystallogr.* **34**, 210–213 (2001)
30. B. Dindar, A.C. Güler, Comparison of facile synthesized N doped, B doped and undoped ZnO for the photocatalytic removal of Rhodamine B. *Environ. Nanotechnol. Monit. Manag.* **10**, 457–466 (2018)
31. J.C. Phillips, Tauc networks and Tauc edges: a review. *J. Non-cryst. Solids* **141**, 1–2 (1992)
32. N.F. Andrade Neto, P.M. Oliveira, M.R.D. Bomio, F.V. Motta, Effect of temperature on the morphology and optical properties of Ag<sub>2</sub>WO<sub>4</sub> obtained by the co-precipitation method: photocatalytic activity. *Ceram. Int.* **45**, 15205–15212 (2019)
33. M. Behboudnia, A. Habibi-Yangjeh, Y. Jafari-Tarzanag, A. Khodayari, Facile and room temperature preparation and characterization of PbS nanoparticles in aqueous [EMIM][EtSO<sub>4</sub>] ionic liquid using ultrasonic irradiation. *Bull. Korean Chem. Soc.* **29**(1), 53–56 (2008)
34. R. Yoo, A.T. Güntner, Y. Park, H.J. Rim, H.-S. Lee, W. Lee, Sensing of acetone by Al-doped ZnO. *Sens. Actuators B* **283**, 107–115 (2019)
35. K. Momma, F. Izumi, VESTA: a three-dimensional visualization system for electronic and structural analysis. *J. Appl. Crystallogr.* **41**, 653–658 (2008)
36. A. Nakrela, N. Benramdane, A. Bouzidi, Z. Kebbab, M. Medles, C. Mathieu, Site location of Al-dopant in ZnO lattice by exploiting the structural and optical characterisation of ZnO: Al thin films. *Results Phys.* **6**, 133–138 (2016)
37. N. Zhang, X. Zou, Y. Gao, Heterovalent cation substitutional and interstitial doping in semiconductor sensitizers for quantum dot cosensitized solar cell. *Int. J. Photoenergy* **2015**, 326850 (2015)
38. M. Liu, Q. Zhan, W. Li, R. Li, Q. He, Y. Wang, Effect of Zn doping concentration on optical band gap of PbS thin films. *J. Alloys Compds.* **792**, 1000–1007 (2019)
39. S.F. Wang, F. Gu, M.K. Lu, Sonochemical synthesis of hollow PbS nanospheres. *Langmuir* **22**, 398–401 (2006)
40. J. Ye, L. Sun, S. Gao, Fabrication of hollow PbS nanospheres and application in phenol release. *SpringerPlus* **2**, 323 (2013)
41. N.F.A. Neto, B.P. Dias, R.L. Tranquilin, E. Longo, M. Li, M.R.D. Bomio, F.V. Motta, Synthesis and characterization of Ag<sup>+</sup> and Zn<sup>2+</sup> co-doped CaWO<sub>4</sub> nanoparticles by a fast and facile sonochemical method. *J. Alloys Compds.* **823**, 153617 (2020)
42. Q. Liang, X. Liu, G. Zeng, Z. Liu, L. Tang, B. Shao, Z. Zeng, W. Zhang, Y. Liu, M. Cheng, W. Tang, S. Gong, Surfactant-assisted synthesis of photocatalysts: mechanism, synthesis, recent advances and environmental application. *Chem. Eng. J.* **372**, 429–451 (2019)
43. S. Asgharzadehahmadi, A.A. Abdul Raman, R. Parthasarathy, B. Sajjadi, Sonochemical reactors: review on features, advantages and limitations. *Renew. Sustain. Energy Rev.* **63**, 302–314 (2016)
44. M. Hassanpour, S.A.H. Tafreshi, O. Amiri, M. Hamadanian, M. Salavati-Niasari, Toxic effects of Fe<sub>2</sub>WO<sub>6</sub> nanoparticles towards microalga *Dunaliella salina*: sonochemical synthesis nanoparticles and investigate its impact on the growth. *Chemosphere* **258**, 127348 (2020)
45. H. Wang, J.-R. Zhang, J.-J. Zhu, Sonochemical preparation of lead sulfide nanocrystals in an oil-in-water microemulsion. *J. Cryst. Growth* **246**, 161–168 (2002)
46. J. Zhu, S. Liu, O. Palchik, Y. Kolytyn, A. Gedanken, A novel sonochemical method for the preparation of nanophasic sulfides: synthesis of HgS and PbS nanoparticles. *J. Solid State Chem.* **153**, 342–348 (2000)

47. M. Molaie, S. Abbasi, M. Karimipour, F. Dehghan, A simple UV-assisted, room temperature approach for synthesis of water soluble PbS and PbS/CdS core–shell QDs. *Mater. Chem. Phys.* **216**, 186–190 (2018)
48. A.L. Stroyuk, A.E. Raevskaya, S.Y. Kuchmii, The effect of PbS nanoparticles on the formation of PbSe in aqueous solutions of sodium selenosulfate and lead(II). *Theor. Exp. Chem.* **42**(6), 346–351 (2006)
49. F.D. Martinez-Mancera, J.L. Hernandez-Lopez, Physical characterization and photoluminescence properties of thioglycolic acid-stabilized lead sulfide nanocrystals. *Mater. Chem. Phys.* **148**, 1045–1054 (2014)
50. D.L. Wood, J. Tauc, Weak absorption tails in amorphous semiconductors. *Phys. Rev. B* **5**(8), 3144–3151 (1972)
51. P. Makuła, M. Pacia, W. Macyk, How to correctly determine the band gap energy of modified semiconductor photocatalysts based on UV–Vis spectra. *J. Phys. Chem. Lett.* **9**, 6814–6817 (2018)
52. V. Krishnakumar, G. Shanmugam, R. Nagalakshmi, Large third-order optical nonlinearity of Mg-doped PbS/PVA freestanding nanocomposite films. *J. Phys. D* **45**, 165102 (2012)
53. A. Sarkar, S. Ghosh, S. Chaudhuri, A.K. Pal, Studies on electron transport properties and the Burstein-Moss shift in indium-doped ZnO films. *Thin Solid Films* **204**, 255–264 (1991)
54. A.A.G. Santiago, N.F. Andrade Neto, E. Longo, C.A. Paskocimas, F.V. Motta, M.R.D. Bomio, Fast and continuous obtaining of Eu<sup>3+</sup> doped CeO<sub>2</sub> microspheres by ultrasonic spray pyrolysis: characterization and photocatalytic activity. *J. Mater. Sci. Mater. Electron.* **30**, 11508–11519 (2019)
55. N.F. Andrade Neto, E. Longo, K.N. Matsui, C.A. Paskocimas, M.R.D. Bomio, F.V. Motta, Photocatalytic properties under sunlight of heterostructures AgCl/CuO obtained by sonochemical method. *Plasmonics* **14**, 79–89 (2019)
56. P.A. Ajibade, A.E. Oluwalana, Synthesis and crystal structure of bis(O-methyl hydrogenato carbonodithioate)–Pb(II): structural, optical and photocatalytic studies of PbS nanoparticles from the complex. *J. Coord. Chem.* **72**, 3575–3588 (2019)
57. C.H. Nguyen, C.-C. Fu, R.-S. Juang, Degradation of methylene blue and methyl orange by palladium-doped TiO<sub>2</sub> photocatalysis for water reuse: efficiency and degradation pathways. *J. Clean. Prod.* **202**, 413–427 (2018)
58. S. Varnagir, A. Medvids, M. Lelis, D. Milcius, A. Antuzevics, Black carbon-doped TiO<sub>2</sub> films: synthesis, characterization and photocatalysis. *J. Photochem. Photobiol. A* **382**, 111941 (2019)
59. W. Wang, M.O. Tadé, Z. Shao, Nitrogen-doped simple and complex oxides for photocatalysis: a review. *Prog. Mater. Sci.* **92**, 33–63 (2018)
60. D. Wang, S. Wang, B. Li, Z. Zhang, Q. Zhang, Tunable band gap of NV co-doped Ca:TiO<sub>2</sub>B (CaTi<sub>5</sub>O<sub>11</sub>) for visible-light photocatalysis. *Int. J. Hydrog. Energy* **44**, 4716–4723 (2019)
61. Z. Li, X. Meng, Z. Zhang, Few-layer MoS<sub>2</sub> nanosheets-deposited on Bi<sub>2</sub>MoO<sub>6</sub> microspheres: a Z-scheme visible-light photocatalyst with enhanced activity. *Catal. Today* **315**, 67–78 (2018)
62. D. Chen, S. Wu, J. Fang, S. Lu, G. Zhou, W. Feng, F. Yang, Y. Chen, Z. Fang, A nanosheet-like α-Bi<sub>2</sub>O<sub>3</sub>/g-C<sub>3</sub>N<sub>4</sub> heterostructure modified by plasmonic metallic Bi and oxygen vacancies with high photodegradation activity of organic pollutants. *Sep. Purif. Technol.* **193**, 232–241 (2018)

**Publisher's Note** Springer Nature remains neutral with regard to jurisdictional claims in published maps and institutional affiliations.